

Numerical and Experimental Investigation into Effect of Temperature Field on Sensitization of Alloy 690 Butt Welds Fabricated by Gas Tungsten Arc Welding and Laser Beam Welding

Hwa Teng Lee^{a*} and Chun Te Chen^b

Abstract

This study examines the effects of the temperature field on the sensitization of Alloy 690 butt welds fabricated using the gas tungsten arc welding (GTAW) method and the laser beam welding (LBW) method, respectively. The welding thermal cycles of the two welding methods are simulated using ANSYS software based upon a moving heat source model and the high-temperature thermal physical property data maintained in the JMatPro database. The validity of the numerical model is confirmed by comparing the simulation results with the corresponding experimental findings. It is found that the agreement between the numerical results for the temperature field and the experimental temperature measurements. In addition, it is shown that the LBW weldment experiences a more rapid heating and cooling effect than the GTAW weldment, and therefore has both a smaller heat-affected zone (HAZ) and a narrower sensitization region. Overall, the simulation results presented in this study are found to be in good agreement with the experimental findings. Thus, the validity and general applicability of the thermal welding model are confirmed.

Keywords: Sensitization, Heat-Affected Zone, Welding Thermal Cycle, Laser Beam Welding, Gas Tungsten Arc Welding, Transient Temperature Field

Hwa Teng Lee / Professor, Department of Mechanical Engineering, National Cheng Kung University, Tainan 701, TAIWAN, ROC.
Chun Te Chen / Ph.D., Department of Mechanical Engineering, National Cheng Kung University, Tainan 701, TAIWAN, ROC.

1. Introduction

Of all the engineering materials in use nowadays, Alloy 600 and Alloy 690 are amongst the most common. The heat exchanger tubes in early nuclear power plants were generally fabricated from Alloy 600 using a gas tungsten arc welding (GTAW) welding process. However, in the late 1980s, it was reported that Alloy 600 is susceptible to pitting, stress corrosion cracking (SCC) and intergranular stress corrosion cracking (IGSCC) as a result of a sensitization effect during cooling in which Cr-rich carbides (e.g. Cr_{23}C_6 and Cr_7C_3) are precipitated at the grain boundaries. As a result, serious doubts were raised as to its suitability for such critical applications as nuclear power plant components by Scott [1] and Harrod et al. [2]. Researchers have generally resolved this safety issue through the use of alternative materials by Kim and Moon [3] (e.g. Alloy 690 with a higher chromium content and lower carbon content than Alloy 600) or the application of more sophisticated welding techniques such as laser beam welding (LBW) or electron beam welding (EBW). Compared to the traditional GTAW welding process, Nd:YAG LBW is characterized by a more concentrated heat input, a higher welding speed and a faster cooling rate. As a result, the weldment has a narrower heat-affected zone (HAZ), a lower residual stress, and a reduced susceptibility to carbide precipitation during cooling. In addition, Nd:YAG LBW has the advantage that the heat energy can be supplied remotely to the welding area via an optic fiber, and thus Kim et al. [4] reported that Nd:YAG LBW is an ideal solution for the repair of components in hazardous environments such as nuclear reactor plants.

Welding is a highly complex physical phenomenon, influenced by many parameters including the heat transmission mode (i.e. conduction, radiation, and convection), the geometry and properties of the workpiece, the phase transformations caused by the heat input in the welding procedure, and so on. In addition, the welding performance is significantly dependent upon the welding parameters, e.g. the voltage, current, choice of electrode, welding speed, and intensity of heat input. Analytical solutions and heat source style for the temperature field induced during welding models [5-9]. Thus, analytical methods are limited in their ability to clarify the physical phenomena which take place during a typical welding operation. Accordingly, recent researchers have generally employed some form of numerical

modeling approach to simulate the welding process. Typical methods include the Finite Element Method (FEM), the Finite Difference Method (FDM) and the Boundary Element Method (BEM). An excellent review of the thermal modeling of laser welding and related processes is provided by Mackwood in [10]. Although various numerical modeling techniques are available, FEM tends to be the most widely used because its convenience [11, 13].

Although computer simulations provide the means to obtain detailed insights into the basic phenomena associated with a variety of welding processes, the accuracy of the simulation results is critically dependent on the values assigned to the physical properties of the workpiece, e.g. the thermal conductivity, the density, the specific heat, and so on. In practice, these properties vary as a non-linear function of the temperature, and thus if the temperature effect is not taken into account, the simulation results will inevitably deviate from the experimental findings. Little and Kamteka [14] investigated the effects of the welding efficiency and the thermal properties of the workpiece on the transitional temperature fields induced during the arc welding process. Since the physical properties of many materials vary non-linearly with the temperature in the high-temperature regime, Zhu and Chao [15] suggested that in the absence of reliable data, welding simulations should take the average value of the thermal conductivity computed over all known temperatures as the working value rather than the room temperature value. In recent years, the problem of accounting for the temperature-dependent nature of the physical properties of engineering materials has been resolved to a large extent through the commercial JMatPro software package [16], which enables the user to obtain the physical properties of a material at any temperature provided that the material's chemical composition is known.

The sensitization range of Alloy 600 extends from 540 to 980 °C, and comprises a Cr_{23}C_6 precipitation range from 540~760 °C and a Cr_7C_3 precipitation range from 760~980 °C [17]. Since Alloy 690 has a lower carbon content than Alloy 600, the sensitization effect is particularly pronounced at temperatures in the range 540~760 °C. Therefore, in improving the corrosion resistance of welded Alloy 690 components, it is essential to develop a detailed understanding of the thermal welding cycles within the weldment in order to predict the susceptibility of the weldment to the sensitization

phenomenon. While the published literature contains many experimental investigations into the microstructure and corrosion resistance properties of Alloy 690 [18,19], and the mechanism of microcracking in the multipass weld metal of alloy 690[20-22], relatively few studies have performed a systematic numerical investigation into the effects of the temperature field on the sensitization of Alloy 690 butt welds such as those used in many nuclear power plant components. Accordingly, the present study performs a series of ANSYS simulations based upon a moving heat source model and the physical property data maintained in the JMatPro database to compare and contrast the welding thermal cycles induced in butt welds fabricated using the GTAW method and the LBW method, respectively, and to investigate the effects of these thermal cycles on the sensitization tendencies of the two weldments. The validity of the numerical model is confirmed by comparing the numerical solutions with the experimental results.

2. Theoretical Model

2.1 Theoretical foundation

In constructing a theoretical model to predict the thermal history of the HAZ during the welding process, the following assumptions are made:

- (1) The workpiece material (Alloy 690) has an austenitic microstructure and undergoes no phase transformation during the welding procedure.
- (2) The thermal history of the HAZ is determined by the effects of conduction , convection and radiation. Moreover, the coefficients of convection and radiation between the workpiece and the environment are assumed to be a constant.
- (3) The welding process is simulated using a full 3-D finite element model, and we simulate the one half models due to symmetry.
- (4) In this paper, we mainly investigate the thermal affect in HAZ of Alloy 690 welding, so the effects of the electric magnetic field in the GTAW process and keyhole phenomenon in the LBW process do not be discussed.

2.2 Mathematical model of heat transmission during welding process

The distribution of the temperature field induced during welding can be expressed by the following energy balance equation:

$$\rho C \frac{\partial T}{\partial t} = \nabla \cdot (k \nabla T) - \rho C \mathbf{U} \cdot \nabla T + \dot{Q}_G, \quad (1)$$

where ρ is the density (kg/m^3), C is the specific heat (J/kg.K), T is the temperature (K), t is time (sec), k is the thermal conductivity (W/m.K), \mathbf{U} is the welding velocity and \dot{Q}_G is the rate of heat generation or consumption per unit volume (W/m^3).

In modeling the heat transmission during welding, the effects of weld pool stirring are ignored. Moreover, k is assumed to be isotropic in all directions. The steady-state heat flow can be modeled using the following energy balance equation:

$$\rho C \frac{\partial T}{\partial t} = k(T) \left\{ \frac{\partial^2 T}{\partial x^2} + \frac{\partial^2 T}{\partial y^2} + \frac{\partial^2 T}{\partial z^2} \right\} + \frac{\partial k}{\partial T} \left\{ \left(\frac{\partial T}{\partial x} \right)^2 + \left(\frac{\partial T}{\partial y} \right)^2 + \left(\frac{\partial T}{\partial z} \right)^2 \right\} + \dot{Q}_G, \quad (2)$$

2.3 Construction of welding model

The analysis performed in this study considers the butt welding of two thin Alloy 690 plates of equal dimensions. During the welding process, the sheets are placed on a stationary work plane with the fixed coordinate system (x, y, z) shown in Fig. 1. The heat supplied to the weldment is provided by a GTAW or a LBW. In each case, the moving heat source is modeled using the moving coordinate system (ξ, y, z) shown in Fig. 1, and is assumed to have a Gaussian heat distribution. During the welding process, the heat source moves continuously in the x -direction of the work plane at a constant velocity u . Thus, the moving heat source q is heat supplied to the weldment can be modeled as $q(\xi, y, z)$, in which $\xi = x + ut$. The corresponding heat transmission can be computed from Equation (2).

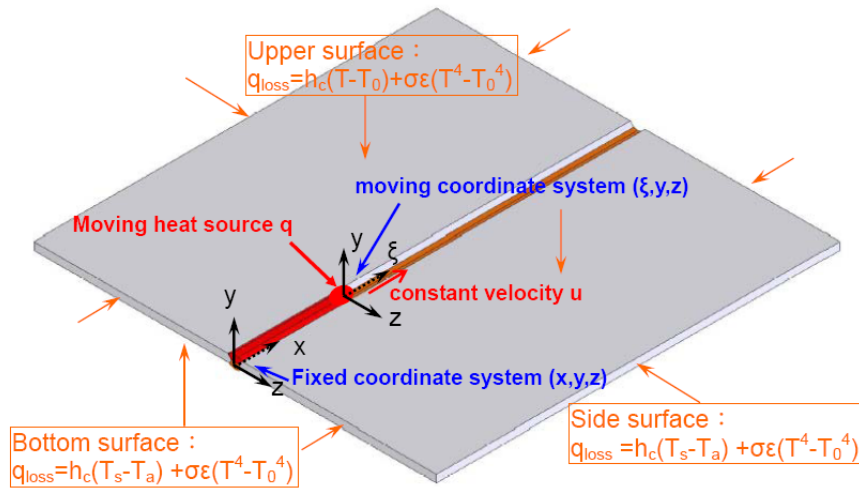


Fig. 1 Weldment coordinate systems with moving heat source

2.4 Initial and Natural boundary condition

The Initial and natural boundary condition imposed in the mathematical welding model comprises two parts, the following conditions apply:

1. Initial condition

$$T(x, y, z, 0) = T_0(x, y, z), \quad (5)$$

2. Natural boundary condition

$$k_n \frac{\partial T}{\partial n} + q + h_c(T - T_0) + \sigma \varepsilon(T^4 - T_0^4) = 0, \quad (6)$$

where k_n is thermal conductivity normal to the surface (W /m C), h_c is the heat transfer coefficient for convection (W/m² C), T_0 is the atmospheric temperature for the convection and/or radiation, σ is the Stefan-Boltzmann constant (W/m²C⁴) and ε is the radiation emissivity.

2.5 Model of welding heat source

In modeling the GTAW and LBW welding process, it is assumed that the electric arc or the laser beam forms moving heat source of Gaussian heat source on the surface of the weldment[6] and double ellipsoid heat source within weldment[9]. The resulting heat distribution is described by the following Gaussian function:

1. Gaussian surface heat flux distribution

$$q(x,z,t) = \frac{3Q}{\pi c^2} \exp\left\{-\frac{3[x+u(\tau-t)]^2}{c^2}\right\} \exp\left(-\frac{3z^2}{c^2}\right), \quad (7)$$

Where Q is the energy input rate (W) and c is the characteristic radius of the heat flux distribution (m).

2. Double ellipsoid heat source distribution

a. Forward ellipsoid heat source distribution

$$q_f(x,y,z,t) = \frac{6\sqrt{3}f_f Q}{abc\pi\sqrt{\pi}} e^{-3[x+u(x-t)]^2/a^2} e^{-3y^2/b^2} e^{-3z^2/c^2}, \quad (8)$$

b. Rear ellipsoid heat source distribution

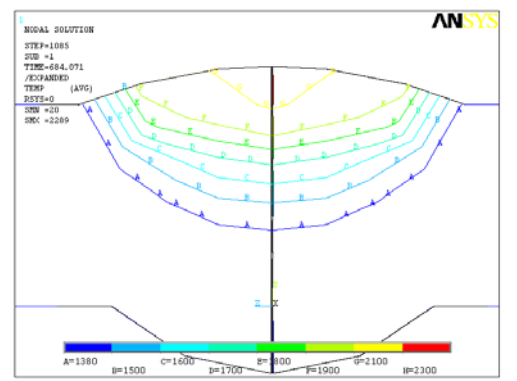
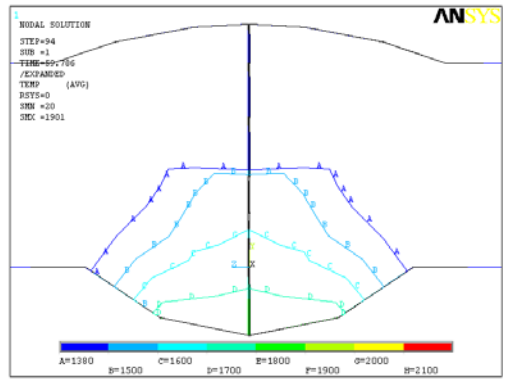
$$q_r(x,y,z,t) = \frac{6\sqrt{3}f_r Q}{abc\pi\sqrt{\pi}} e^{-3[x+u(x-t)]^2/a^2} e^{-3y^2/b^2} e^{-3z^2/c^2}, \quad (9)$$

and

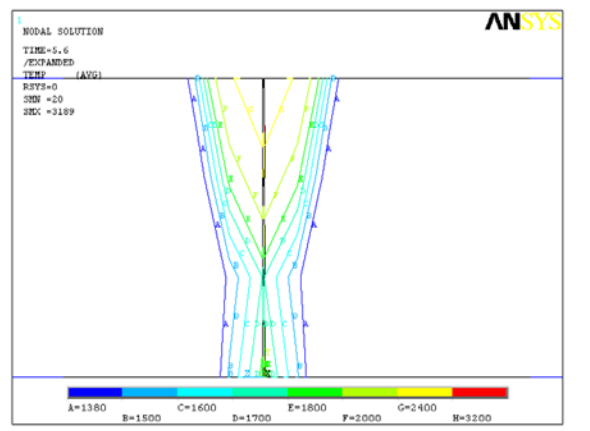
$$f_f + f_r = 2, \quad (10)$$

Where Q =energy input rate (W), a , b and c are the characteristic radius of flux distribution (m), f_f is the energy fraction of the forward part, f_r is the energy fraction of the rear part.

Double ellipsoid heat source was employed in GTAW model and The combined heat source model (surface heat source and double ellipsoid heat source) was employed in LBW model and the temperature distribution caused moving heat source in the fusion zone as shown in Figs. 2(a), 2(b) and 2(c).



- (a) The temperature distribution caused heat of GTAW
 (b) The temperature distribution caused flux in 1st pass of GTAW
 heat flux in 2nd pass of GTAW



- (c) The temperature distribution caused heat flux in LBW

Fig. 2 The temperature distribution caused heat flux in the fusion zone

3. Experimental Procedure

3.1 Welding experiments

The GTAW and LBW butt weldments were fabricated using Alloy 690 plates with a thickness of 3 mm. The plates were supplied by Sumitomo Metal Technology, Hyogo, Japan and had been solution annealed (SA) at a temperature of 1050 °C for 5 minutes and then quenched in water prior to delivery. The chemical composition of the Alloy 690 plates is summarized in Table 1. The as-received plates were machined into specimens measuring 60 × 150 mm² (length × width) and were then polished using 600-grit SiC paper to remove any impurities and oxidized film from their surfaces. Finally, the plates were degreased using an acetone solution. The GTAW butt weld comprised two beveled Alloy 690 plates clamped in such a way as to form an 80° V-groove with a 2.4 mm root opening gap and a 1 mm root face. The weldment was fabricated using a direct current straight polarity (DCSP) GTAW process and was accomplished using two welding passes. The welding process was performed using Alloy 52 filler metal wire with a core diameter of 2.4 mm. The composition of Alloy 52, as determined in accordance with the AWS A5.14 ERNiCr-7 specification, is summarized in Table 2.

The two welding passes were conducted using the process parameters shown in Table 3 with a pure argon (99.9%) shielding gas in both cases.

The LBW weldment comprised two flat-edged Alloy 690 plates positioned in contact with one another along their longest edges and arranged such that their contact interface was aligned with a square groove running the length of a lower support plate. The LBW process was performed without filler metal using a numerical control (NC) Rofin-Sinar CW025 Nd:YAG laser system with a maximum mean power of 2.5 kW. The weldments were fabricated with the laser system set in its pulse wave (PW) mode with a constant mean power of 1750 W, a peak-power (P_p) to base-power (P_b) ratio of 3:2, and a welding speed of 800 mm/min (see Table 3). The frequency and duty cycle of the modulated laser beam were specified as 100 Hz and 50%, respectively. In the welding process, the Nd:YAG laser energy was transmitted through an optical fiber with a diameter of 600 μm and was focused on the upper surface of the workpiece using a lens with a focal length of 120 mm. The weldments were fabricated using pure nitrogen as both the face shielding gas (flow rate: 20 L/min) and the back shielding gas (flow rate: 10 L/min). The face shielding gas was supplied through a copper nozzle with an internal diameter of 4 mm orientated at an angle of 25° to the workpiece surface and positioned 10 mm behind the rear part of the weld pool, while the back shielding gas was delivered through a nozzle positioned parallel to the workpiece surface.

The temperature distributions within the GTAW and LBW weldments were measured continuously throughout the welding process using K-type thermocouples with a diameter of 0.127 mm (AWG No. 36). As shown in Figs. 3(a), 3(b) and 3(c), the thermocouples were attached to the lower surface of the weldments in order to avoid the effects of direct thermal radiation from the welding heat source and were arranged in such a way that the localized temperature gradients and thermal histories could be computed in various regions of interest within the weldment (e.g. the coarse grain zone, the weld decay zone, and the base metal). The thermocouple outputs were sampled every 100 ms and were saved to a PC for further processing.

Table. 1 Chemical composition of Alloy 690 (wt%).

Ni	Cr	Fe	Mn	Ti	C	Si	Cu	P	S	Co
59.05	29.45	Bal.	0.29	0.28	0.019	0.33	0.02	0.01	0.001	0.014

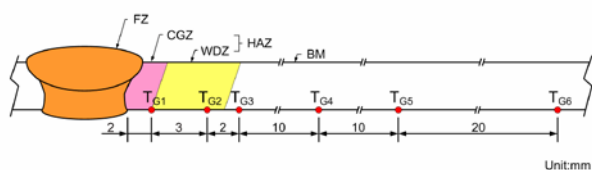
Table. 2 Chemical composition of Inconel Filler Metal 52 (I-52) (wt%).

Ni	Cr	Fe	Mn	Ti	C	Si	Cu	P	S	Al
60.39	28.91	8.89	0.25	0.51	0.03	0.16	0.01	0.003	0.001	0.64

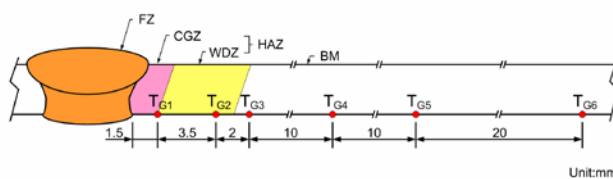
Table. 3 Welding parameters for GTAW and LBW weldments.

GTAW	Voltage	Current	Welding speed (mm/min)
	(V)	(A)	
1 st	15	90	84
2 nd	15	90	108

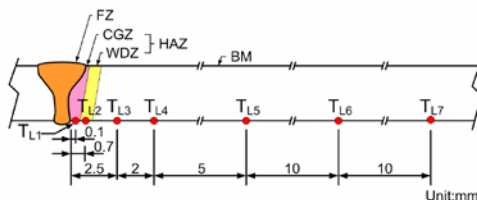
LBW	Waveform	Average power	Welding speed (mm/min)
		(W)	
	PW	1750	800



(a) 1st pass of GTAW



(b) 2nd pass of GTAW



(c) LBW

Fig. 3 Schematic illustration showing temperature measurement positions on [25]:

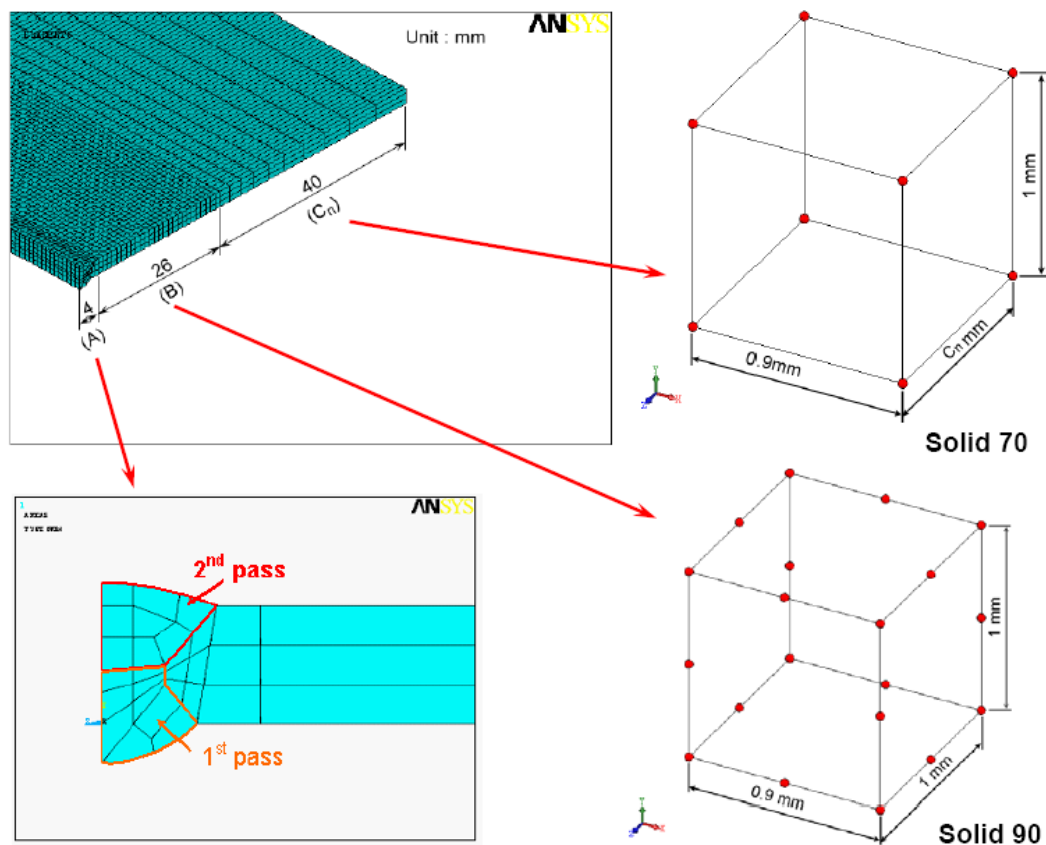
3.2 Numerical simulation of GTAW and LBW welding processes

The temperature fields induced during the GTAW and LBW welding processes were simulated using ANSYS software [24] based upon the time-step parameters given in Table 4 and the finite element models presented in Fig. 4(a) and (b). The two models were constructed using both eight- and twenty-nodal thermal conduction solid elements. In both cases, a fine mesh (3-D 20-node thermal element SOLID90) was used in the regions of the weldment subject to a higher temperature gradient (i.e. close to the welding center line), while a coarse mesh (3-D eight node thermal element SOLID70) was applied elsewhere. In practice, a finer mesh size is required to capture the temperature distribution induced by a smaller heat source. Thus, the GTAW weldment (with a relatively large spot size) was meshed using a grid comprising 24660 elements and 102669 nodes, while the LBW weldment (with a far smaller spot size) was meshed using a grid comprising 26325 elements and 113098 nodes. The function of Element Birth and Death was employed to simulate temperature field in filled metal GTA welding. In the simulations, the ambient temperature and initial workpiece temperature were both specified as 20°C and the heat convection coefficient between the weldment and the ambient environment was assumed to be 60 J°C/m². Finally, the heat convection coefficient between the weldment and the face shielding gas was specified as 120 J°C/m². As discussed in Section 1, the specific heat, thermal conductivity and density of most engineering materials vary as a non-linear function of the temperature. Accordingly, in the present simulations, the thermal physical properties of the Alloy 690 plates and the I52 filler metal were specified in accordance with the profiles shown in Figs. 5(a) and 5(b), respectively, taken directly from the JMatPro database.

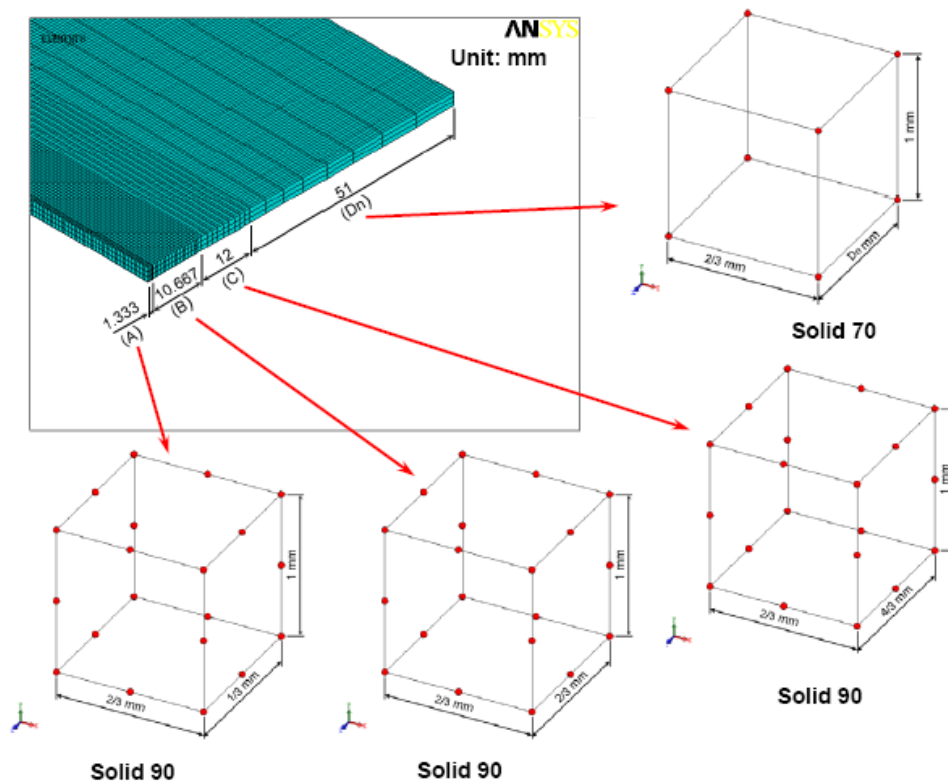
Table. 4 Time-step data used in GTAW and LBW simulations

	Heat source travel speed (Experimental) (mm/min)	Time-step (Simulation) (mm) / (sec)	Heat input (Experimental) (J/mm)	Heat input (Simulation) (J/mm)

GTAW	1 st	84	(0.9)/(0.64)	964.3	540.43
	2 nd	108	(0.9)/(0.5)	750	396.05
LBW		800	(0.667)/(0.05)	131.25	90.13

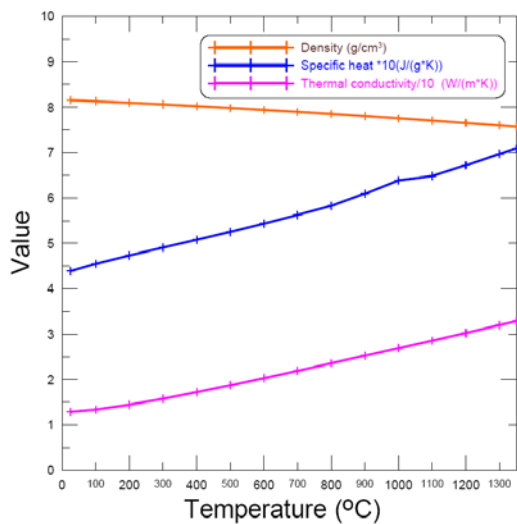


(a) GTAW mesh

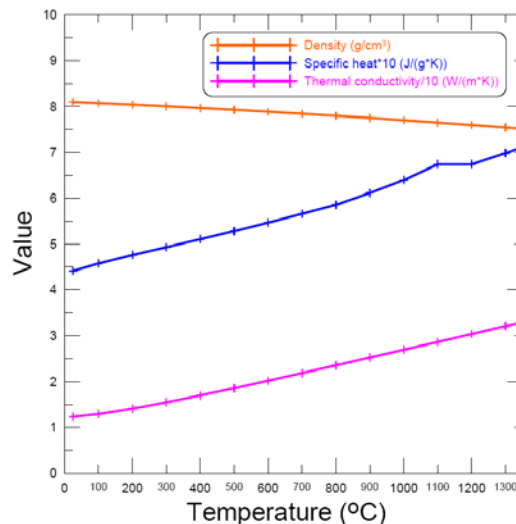


(b) LBW mesh

Fig. 4. FEM meshes of GTAW and LBW weldments used in ANSYS simulations



(a) Thermal properties of Alloy 690



(b) Thermal properties of I52 filler metal

Fig. 5. Thermal properties of Alloy 690 base material and I51 filler metal [16]

4. Results and Discussions

4.1 Comparison of peak temperatures in different regions of weldment

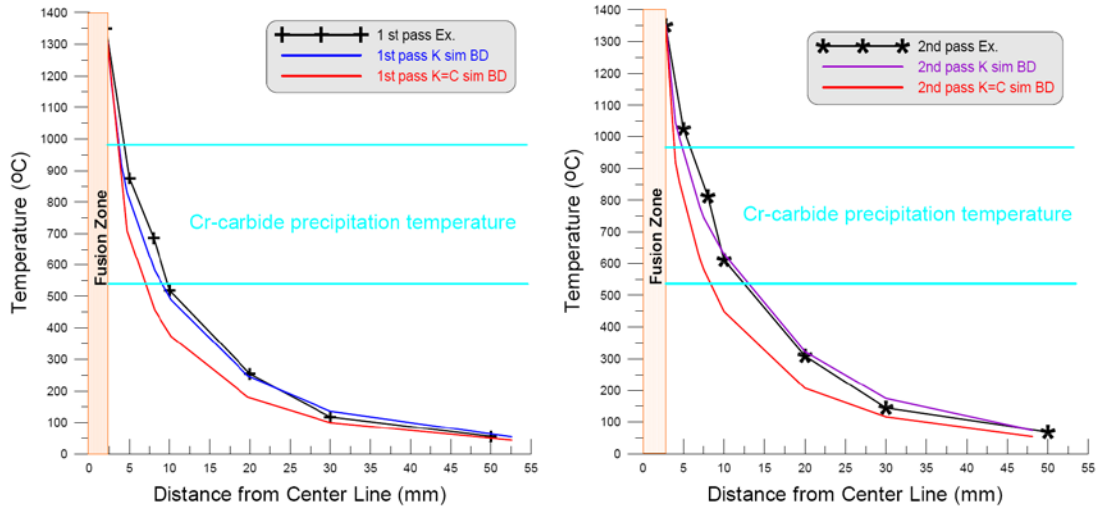
In accordance with the heat conduction formula given in Equation (2), it can be seen that the temperature gradient within the weldment is determined by the thermal conductivity k , specific heat C , and density ρ , which gained from Fig. 5.(a) and 5(b). Figs. 6(a), 6(b) and 6(c) present the numerical and experimental results obtained for the transient temperature fields within the GTAW and LBW weldments, respectively. Note that in three figures, the simulation results are computed using various values of the thermal physical property (Figs. 5(a) and 5(b)) and are compared with the experimental measurements obtained at equivalent positions within the weldment.

The welding speed in the GTAW process (i.e. 84 mm/min in the first pass and 108 mm/min in the second pass, see Table 3) is significantly slower than that in the LBW process (i.e. 800 mm/min). Consequently, the GTAW weldment receives a greater heat input than the LBW weldment and cools more slowly. Therefore, comparing the three figures (6(a), 6(b) and 6(c)), it is observed that the temperature profiles associated with the GTAW weldment have a smaller gradient than those of the LBW weldment. In Fig. 6, it is observed that the optimal agreement between the simulation results and the experimental measurements is obtained.

In addition, in Figs. 6(a) , 6(b) and 6(c), the curves labeled “ $k = C$ ” depict the simulation results obtained when computing the temperature field using constant values of the heat conduction coefficient k , specific heat C , and density ρ derived at room temperature (20 °C). In other words, the two curves represent a linear rather than non-linear simulation result. It is observed that three profiles deviate to a greater or lesser extent from the experimental temperature fields. Thus, the importance of taking the temperature-dependent nature of the physical properties into account when simulating the welding process is confirmed. The deviation of temperature in LBW is less than GTAW.

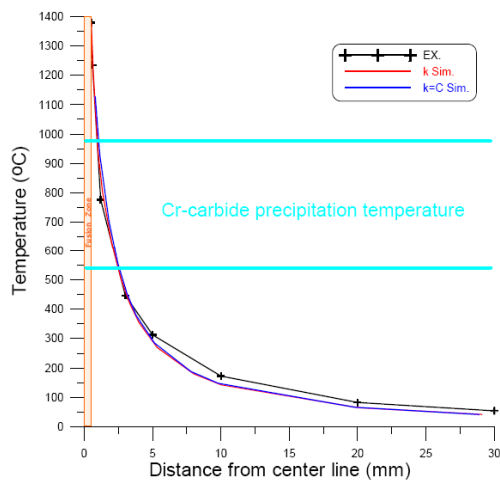
As discussed in Section 1, Alloy 690 is particularly prone to a sensitization effect at temperatures in the range 540~760 °C. In practice, the amount of carbide phase precipitated within the HAZ of the

weldment depends on the time for which the weldment remains within this temperature range during the cooling stage of the welding process. As shown in Figs. 6(a) , 6(b) and 6(c), the LBW weldment cools more rapidly than the GTAW weldment, and thus it can be inferred that the LBW weldment has an improved IGC resistance.



(a) Peak temperature profiles of 1st pass in GTAW weldment

(b) Peak temperature profiles of 2nd pass in GTAW weldment



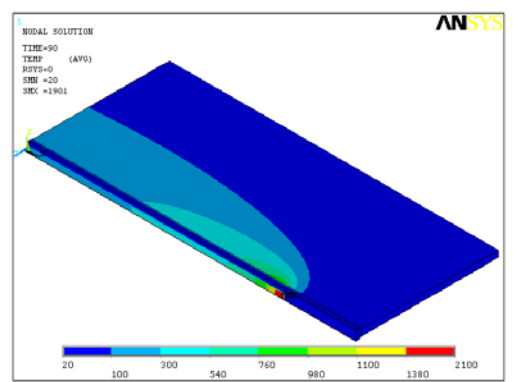
(c) Peak temperature profiles in LBW weldment

Fig. 6 Peak temperature profiles in GTAW and LBW weldments

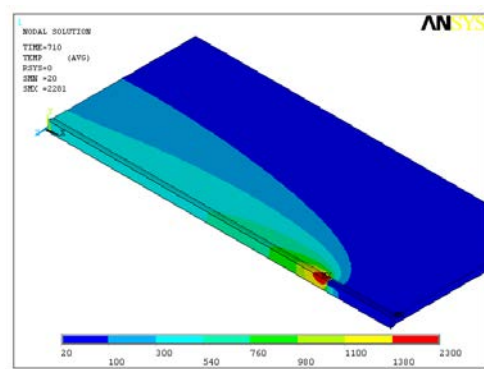
4.2 Transient temperature field and cross-sectional morphology of weld

Fig. 7 presents snapshots of the simulated temperature field within the GTAW weldment after 90th and

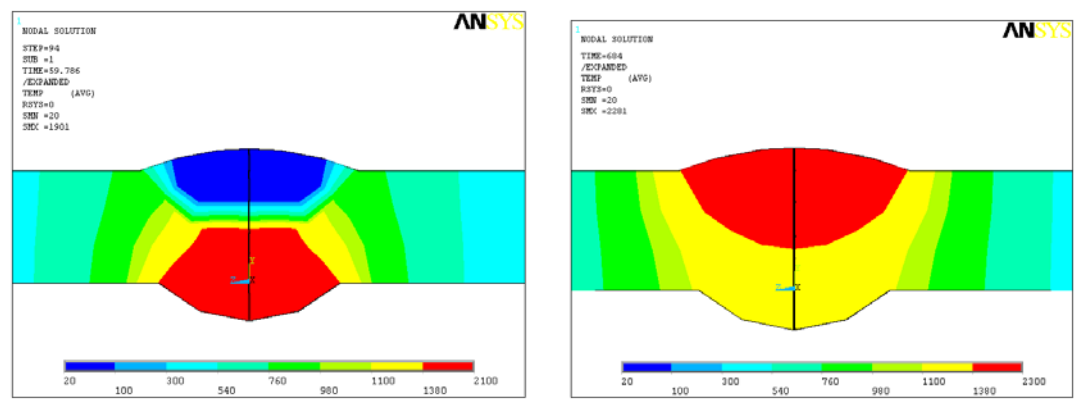
710th second, respectively, and shows the cross-sectional morphology of the corresponding experimental weld. Note that in the simulation images, the red region represents the temperature above 1380 °C (i.e. the melting point of Alloy 690 [16]), and therefore corresponds to the fusion zone (FZ) of the weld. Due to the assumption of a quasi-steady state welding process (see Section 4.1), the distribution of the temperature field contours in the y-direction of Fig. 7(a) (corresponding to the 90th time unit) are virtually identical to those in Fig. 7(b) (corresponding to the 710th time unit). In general, the color contours in the simulation images provide a convenient means of predicting the extent of the HAZ within the weldment. For example, in Figs 7(f), the pale green regions, corresponding to a temperature range of 540~760 °C mark the extent of the sensitization region of the HAZ. Fig. 7(c) and 7(d) present the transverse cross-section of simulated transient temperature field in 1st and 2nd pass of GTAW. From inspection, the width of the FZ (as indicated by the red regions in Fig. 7(c) and (d)) is found to be 5.6 mm. As shown in the OM image presented in Fig. 7(e), the weld root is approximately 5.6 mm. In other words a good agreement is observed between the two sets of results, and hence the validity of the numerical model in predicting the size of the weld cross-section is confirmed.



(a) Transient temperature field in 90th second

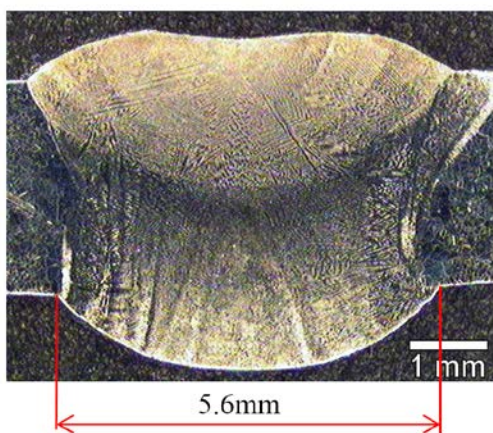


(b) Transient temperature field in 710th second

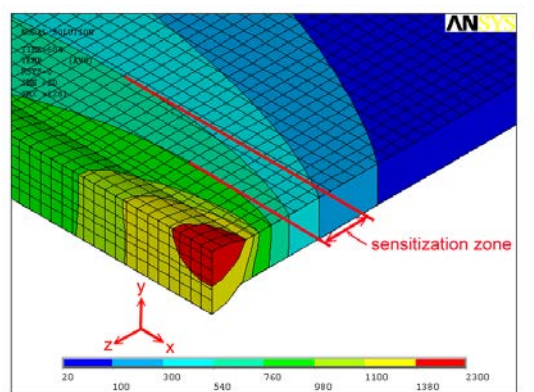


(c) Transverse cross-sectional view of 1st pass GTAW weldment in simulation

(d) Transverse cross-sectional view of 2nd pass GTAW weldment in simulation



(e) Transverse cross-sectional view of weldment

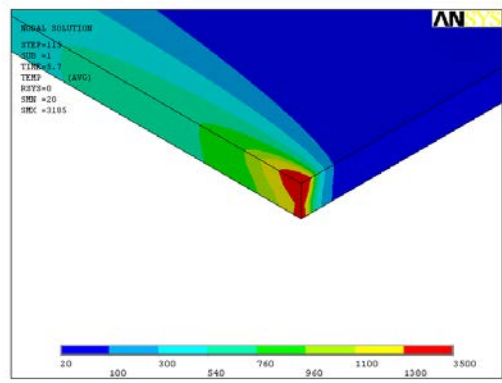


(f) Sensitization zone of 2nd pass GTAW in transient temperature field

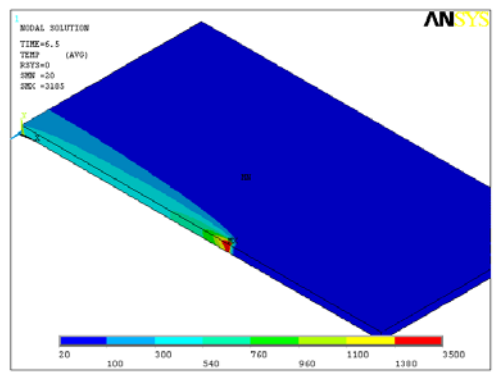
Fig. 7 Transient temperature fields in GTAW weldment and cross-sectional morphology of GTAW weldment

Figs. 8(a) and 8(b) present the simulated transient temperature fields within the LBW weldment after 5.7th second and 6.5th second, respectively. Compared with the images presented in Figs. 7(a) and 7(b), respectively, it is clear that the LBW weldment has both a smaller HAZ and a narrower sensitization region. From an inspection of Figs. 8(c) and 8(d), the width of the weld root is determined to be of the order of 0.67 mm. In addition, the results show that the sensitization zone has a width of approximately 4.5 mm ($-z=8\sim 12.5$ mm) in the GTAW weldment(Fig. 7(f)), but just 1 mm

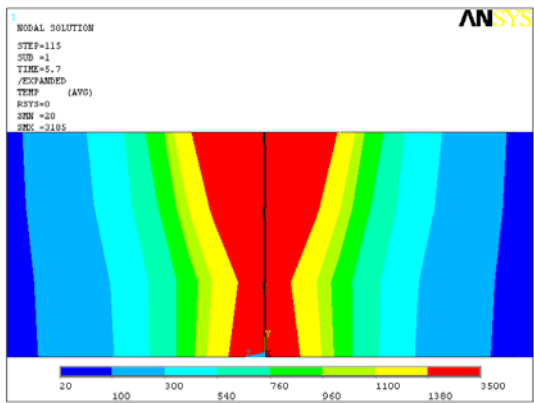
(-z=1~2 mm) in the LBW weldment(Fig. 8(e)).



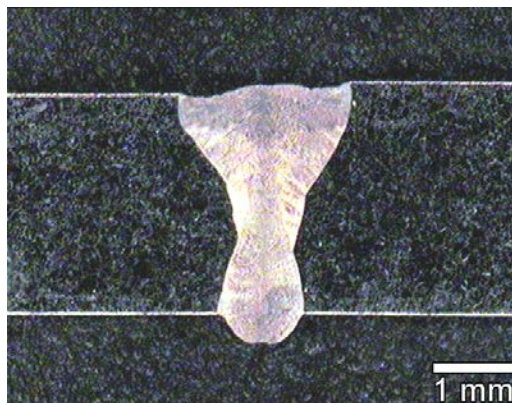
(a) Transient temperature field at 5.7th second



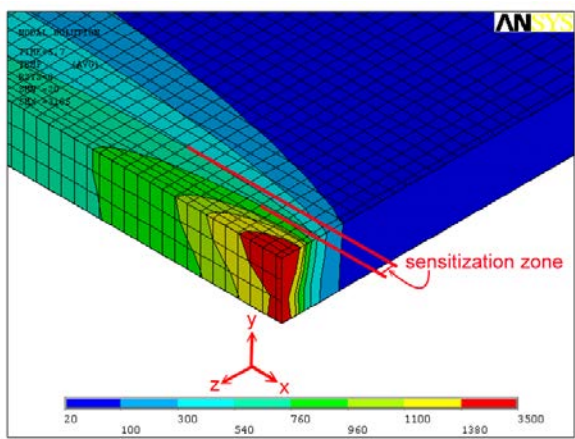
(b) Transient temperature field at 6.5th second



(c) Transverse cross-sectional view of LBW in simulation at 5.7th second



(d) Transverse cross-sectional view of LBW weldment



(e) Sensitization zone of LBW in transient temperature field

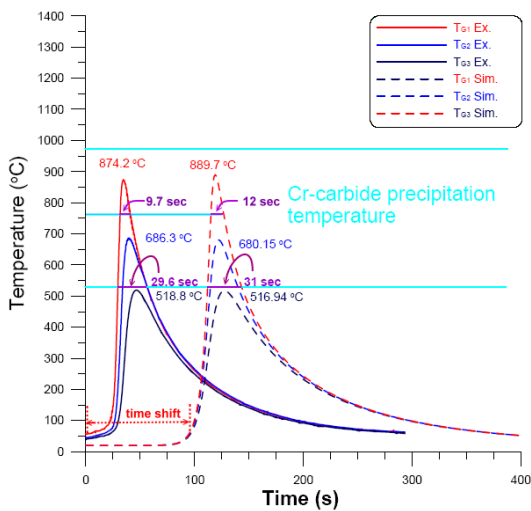
Fig. 8 Transient temperature fields in LBW weldment and cross-sectional morphology of LBW weldment

4.3 Temperature history of HAZ in different regions of weldment

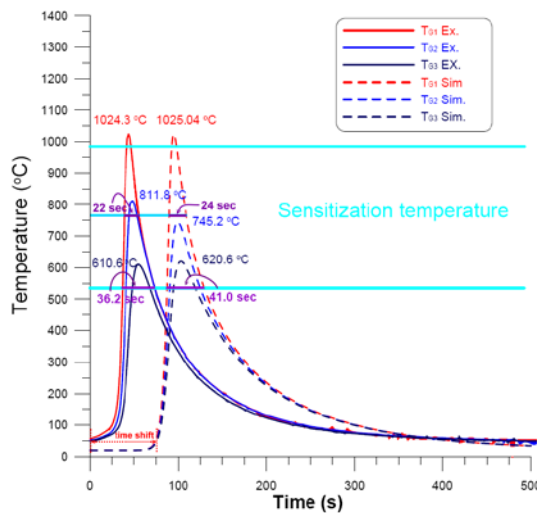
Figs. 9(a) and 9(b) present the experimental and simulated thermal histories, respectively, for the three mainly measurement positions on the 1st and 2nd pass of GTAW weldment. Observing the profiles corresponding to measurement position T_{G1} in 9(a) and 9(b) located in the sensitization region of the weldment, they are seen that the maximum experimental temperature are 889.7 °C and 1024.3 °C while the corresponding simulation values are 874.2 °C and 1025.04 °C. In other words, the maximum simulated temperature deviates from the experimental value by less 3%. In 1st pass cases (in Fig 9(a)), In the case of the experimental results, the corresponding region of the weldment cools through the sensitization range in approximately 19.9 seconds (i.e.(29.6-9.7)), and thus the cooling rate is found to be around 11.1 °C/sec (i.e. (760-540)/19.9). In the case of the simulation results, Fig. 9(a) shows that the corresponding the cooling rate is 11.6 °C /sec, and the time within the sensitization range is 19 seconds. In 2st pass cases (in Fig 9(b)), In the case of the experimental results, the corresponding region of the weldment cools through the sensitization range in approximately 14.2 seconds, and thus the cooling rate is found to be around 15.5 °C/sec. In the case of the simulation results, Fig. 9(b) shows that the corresponding the cooling rate is 13 °C /sec, and the time within the sensitization range is 17 seconds. Though the cooling rate of 2nd pass is higher than 1st pass, the sensitization of GTAW is emphasized in 2nd pass, because the time of Cr-rich carbides precipitated is accumulative.

In the experimental results presented in Fig. 9(b), it can be seen that the maximum temperature at measurement position T_{G2}, located at the far-most extremity of the sensitization region, is around 812 °C. Moreover, the cooling rate is found to be 12 °C/sec, and thus this particular region of the weldment cools through the sensitization range in approximately 19 seconds. In the case of the simulation results, Fig. 9(b) shows that the corresponding maximum temperature is 745.2 °C, the cooling rate is 6.8 °C /sec, and the time within the sensitization range is 30 seconds. The difference in the two sets of results for this measurement position is thought to the result of a slight positioning error when attaching the thermocouple to the undersurface of the weldment. Since this region of the weldment is close to the

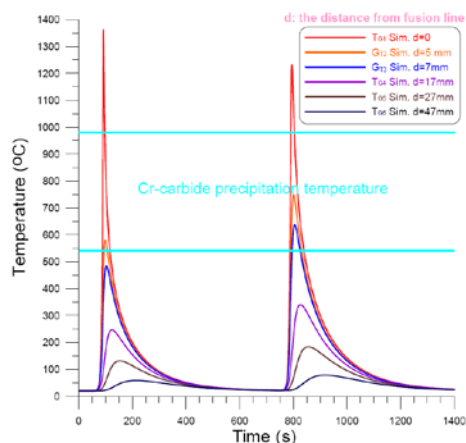
weld, it experiences a large temperature gradient, and thus even very small positioning errors result in a significant difference in the measured temperature value. At a greater distance from the weld, the sensitivity of the experimental temperature measurement to positioning errors reduces as a result of the lower temperature gradient. Consequently, a better agreement is observed between the experimental results and the simulation results for the peak temperature at measurement position T_{G3} in Fig 9(a) i.e. 518.8°C and 516.94°C and Fig 9(b) i.e. 610.6°C and 620.6°C , respectively. However, there are little difference exists between the experimental cooling rates and the simulated cooling rates at temperature measurement positions T_{G4} , T_{G5} and T_{G6} and they are not so demand to be discussed because their position are not in sensitization zone. We combine welding thermal cycles of 1st and 2nd pass of GTAW as Fig 9(c).



(a) Experimental and numerical results of thermal cycles in 1st pass of GTAW



(b) Experimental and numerical results of thermal cycles in 2nd pass of GTAW



(c) Combination of welding thermal cycles in 1st and 2nd pass of GTAW

Fig. 9 Experimental and numerical results for thermal histories at various positions of GTAW weldment

Figs. 10 presents the experimental and simulated thermal histories, respectively, for the four measurement positions on the LBW weldment. In Fig. 10, the peak experimental temperatures at measurement positions T_{L1} and T_{L2} , both located within the sensitization region of the weldment, are found to be 1234.8 °C and 776.1 °C, respectively. Meanwhile, the cooling rates at T_{L1} and T_{L2} are determined to be 157 °C/sec and 147 °C/sec. As a result, the corresponding regions of the weldment cool through the sensitization range within 1.4 seconds and 1.5 seconds, respectively. Fig. 10 shows that the peak simulated temperature values at measurement positions T_{L1} and T_{L2} are 1242.65 °C and 757.3 °C, respectively. The cooling rates at T_{L1} and T_{L2} are found to be 174.6 °C/sec and 125.3 °C/sec, respectively. Thus, the corresponding regions of the weldment cool through the sensitization range in approximately 1.4 and 1.7 seconds, respectively. From inspection, the simulation results for the peak temperature in the LBW weldment deviate from the experimental values by no more than 3%. The slightly higher values of the cooling rates in experimental values compared to those simulated values in Fig. 10 are to be expected since it is reasonable to expect the actual heat conduction of the workpiece material to be somewhat less than the value assumed in the simulations.

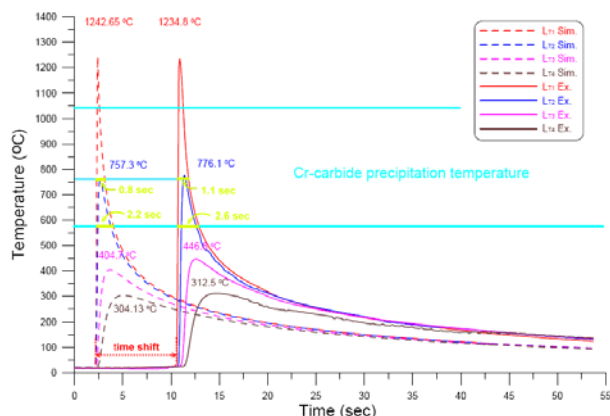


Fig.10 Experimental and numerical results for thermal histories at various positions of LBW weldment

Comparing Figs. 9 and 10, it is seen that the area under the temperature profiles in the LBW weldment is significantly less than that under the temperature profiles in the GTAW weldment. Furthermore, the temperature gradients induced by the LBW process are greater than those induced by the GTAW process. Thus, the two figures confirm that the LBW process results in a lower total heat input to the weldment and a more rapid heating and cooling effect. As a result, the LBW weldment has both a narrower HAZ than the GTAW weldment and a lower susceptibility to sensitization (i.e. an improved IGC resistance).

5. Conclusions

Utilizing a composite heat source model and the high-temperature physical property data derived using JMatPro software, this study has performed a numerical investigation into the temperature fields induced within GTAW and LBW weldments in order to better understand their respective sensitization tendencies. The validity of the numerical model has been confirmed by comparing the simulation results with the corresponding experimental results. The major findings of this study can be summarized as follows:

1. In general, a good agreement exists between the experimental and simulation results for the peak temperature and time duration within the sensitization range in different regions of the GTAW and LBW weldments.

2. When specifying the thermal physical property from the JMatPro database in the thermal welding model, the simulated temperature fields deviate less from the experimental temperature fields. The optimal agreement between the two sets of results is obtained in the simulated GTAW welding process and the LBW welding process.
3. The experimental and simulation results have shown that the area enclosed by the temperature field contours in the LBW weldment is less than that enclosed by the temperature field profiles in the GTAW weldment. Furthermore, the temperature gradients in the LBW weldment are steeper than those in the GTAW weldment. In other words, the results show that the LBW weldment receives a lower total heat input than the GTAW weldment and experiences a more rapid heating and cooling effect. As a consequence, both the overall size of the HAZ and the width of the sensitization region are smaller in the LBW weldment than in the GTAW weldment.
4. The FEM models we use can help us easily find the sensitization zone of Alloy 690 weldments. So we can estimate that the range and size of sensitization zone and the time duration of sensitization temperature in the GTAW weldment and LBW weldment.

Acknowledgments

The authors gratefully acknowledge the financial support of National Science Council, Taiwan (ROC), under Contract No. NSC 96-NU-7-006-001.

References

- [1] Scott, P.M., 2007. An overview of materials degradation by stress corrosion in PWRs Edited by D Féron, CEA-Saclay and J-M Olive Corrosion Issues in Light Water Reactors: Stress Corrosion Cracking. Woodhead England, 3–24.
- [2] Harrod, D.L., Gold, R.E., Jacko, R.J., 2001. Alloy optimization for PWR steam generator heat-transfer tubing. JOM. 53, 14–7.
- [3] Kim, J.D., Moon, J.H., 2004. C-ring stress corrosion test for Inconel 600 and Inconel 690 sleeve joint welded by Nd:YAG laser. Corros. Sci. 46, 807–818.
- [4] Kim, J.D., Kim, C.J., Chung, C.M., 2001. Repair welding of etched tubular components of nuclear power plant by Nd:YAG laser. J. Mater. Process. Technol. 114, 51–56.
- [5] Rosenthal, D., 1946. The theory of moving sources of heat and its application to metal treatments. Trans ASME 68, 849–866.
- [6] Pavelic, V., Tanbakuchi, R., Uyehara O.A., Myers, P.S. 1969. WJ Supplements 48, 295s–305s.

- [7] Friedman, E., 1975. J. Pressure Vessel Technol.—Trans. ASME ASME 97, 206–213.
- [8] Krutz, G.W., Segerlind, L.J., 1978. WJ. Supplements 57, 211s–216s.
- [9] Goldar, J., Chakravarti, A., Bibby, M., 1984. A New Finite Element Model for Welding Heat Source. Metall. Trans. B 15, June 299–305.
- [10] Mackwood, A.P., Crafer, R.C., 2005. Thermal modelling of laser welding and related processes: a literature review. Opt.Laser Technol. 37, 99–115.
- [11] Lu F., Yao S., Lou, S., Li, Y., 2004. Modeling and finite element analysis on GTAW arc and weld pool. Comput. Mater. Sci. 29, 371–378.
- [12] Shan, X.Y., Tan, M.J., O’Dowd N.P. 2007. Developing a realistic FE analysis method for the welding of a NET single-bead-on-plate test specimen. J. Mater. Process. Technol. 192, 497–503.
- [13] Kuo, H.C., Wu, L.J., 2002. Prediction of heat-affected zone using Grey theory. J. Mater. Process. Technol. 120, 151–168.
- [14] Little, G.H., Kamtekar, A.G., 1998. The effect of thermal properties and weld efficiency on transient temperatures during welding. Comput. Struct. 68, 157–165.
- [15] Zhu, X.K., Chao, Y.J., 2002. Effects of temperature-dependent material properties on welding simulation. Comput. Struct. 80, 967–976.
- [16] J MatPro 4.1, Thermotech Sente Software_ 2007. Available from:<http://www.Thermo-tech.co.uk/>.
- [17] INCONEL®alloy 600 Technical Bulletin”, <http://www.specialmetals.com>.
- [18] Kuo, T.Y., Lee, H.T., 2002. Effects of filler metal composition on joining properties of alloy 690 weldments. Mater. Sci. Eng. A 338, 202–212.
- [19] Lee, H.T., Lin, Y.D., Kuo, T.Y., Jeng, S.L. 2007. Precipitated phases and corrosion behavior in the dissimilar alloy 690-SUS 304L joints formed by EBW and GTAW. Mater. Trans. 48, 1538–1547.
- [20] Dieter Radaj, 1992. Heat Effects of Welding. Springer-Verlag.
- [21] Masubuchi, K. 1980. Analysis of Welded Structures. Pergamon Press, Oxford, UK.
- [22] Sindo Kou 1987. Welding Metallurgy. John Wiley & Sons.
- [23] Zacharia, T., David, S.A., Vitck, J.M., Debroy, T., 1989. Metall. Trans.A 20, 957–967.
- [24] ANSYS, Inc, Southpointe 275 Technology Drive Canonsburg, PA 15317.
- [25] Lee, H.T., Wu, J.L., 2009. Correlation between corrosion resistance properties and thermal cycles experienced by gas tungsten arc welding and laser beam welding Alloy 690 butt weldments. Corros. Sci. 51, 733-743.
- [26] Lee, H.T., Wu, J.L., 2009. The effects of peak temperature and cooling rate on the susceptibility to intergranular corrosion of alloy 690 by laser beam and gas tungsten arc welding. Corros. Sci. 51, 439–45.